Oxygen-carrying nanoplatform to reprogram tumor immunosuppressive microenvironment and enhance photothermal-immunotherapy

Ju Huang [a,1], Xiaojing Leng [a,1], Tao Jiang [b], Lihong Xu [c], Jun Zheng [a], Mingxiao Fang [a], Jingxue Wang [a], Zhigang Wang [a,**], Liang Zhang [a,d,*]

[a] State Key Laboratory of Ultrasound in Medicine and Engineering, Chongqing Key Laboratory of Ultrasound Molecular Imaging, Department of Ultrasound, The Second Affiliated Hospital of Chongqing Medical University, Chongqing 400010, PR China
[b] Department of Anesthesia, The Affiliated Hospital of Southwest Medical University, Luzhou 646000, PR China
[c] Institute of Life Sciences, Chongqing Medical University, Chongqing 400016, PR China
[d] Department of Ultrasound, The First Affiliated Hospital of Chongqing Medical University, Chongqing 400042, PR China

ARTICLE INFO

ABSTRACT

Immunotherapy shows great promise on treating tumors. However, insufficient antigen exposure and immunosuppressive tumor microenvironment (TME) caused by hypoxia impose a serial of constraints on the therapeutic efficacy. In this study, we developed an oxygen-carrying nanoplatform loaded with perfluorooctyl bromide (PFOB, a second-generation of perfluorocarbon-based blood substitute), IR780 (a photosensitizer) and imiquimod (R837, an immune adjuvant) to reprogram immunosuppressive TME and reinforce photothermal-immunotherapy. The obtained oxygen-carrying nanoplatforms (abbreviated as IR-R@LIP/PFOB) show highly efficient oxygen release behavior and excellent hyperthermia performance upon laser irradiation, thus achieving the attenuation of the inherent tumor hypoxia and the exposure of tumor associated antigens *in situ*, and transforming the immunosuppressive TME to an immunosupportive one. We found that the photothermal therapy of IR-R@LIP/PFOB together with anti-programmed cell death protein-1 (anti-PD-1) would elicit a robust antitumor immunity by increasing the tumor-infiltrating frequencies of cytotoxic CD8^{+} T cells and tumoricidal M1-phenotype macrophages, while reducing immunosuppressive M2-phenotype macrophages and regulatory T cells (Tregs). This study presents these oxygen-carrying IR-R@LIP/PFOB nanoplatforms are potent in removing some negative impacts of immunosuppressive TME caused by hypoxia, and suppressing tumor growth by initiating antitumor immune responses, especially in combination with anti-PD-1 immunotherapy.

1. Introduction

Tumor immunotherapies, including immune checkpoint blockade (*eg.*, PD-1/PD-L1 blockade (PD-1: programmed cell death protein-1; PD-L1: programmed death protein ligand-1)), chimeric antigen receptor T cell (CAR-T) therapy, *etc.*, have been rapidly developed as a next-generation antitumor therapeutic strategy, showing great promise [1–3]. However, some immunotherapies only provoke limited immune responses [4,5]. One reason for the relatively weak response is insufficient antigen exposure, which would lead to the curbed infiltration of

cytotoxic T lymphocytes in solid tumors [6,7]. Another common reason is that the immunosuppressive tumor microenvironment (TME), which typically consists of immunosuppressive molecules, matrix components, and immunosuppressive immune cells, significantly suppresses antitumor immune responses [8–11]. Therefore, increasing antigen exposure and simultaneously modulating immunosuppressive TME could be crucial to improve the immunotherapeutic effect.

Among various strategies to increase antigen exposure, photothermal therapy (PTT) is a promising modality and technique due to its non-invasiveness and relatively less toxic side effects [12–15]. PTT utilizes

the near-infrared (NIR) laser-induced heat-generating ability of photosensitizers to generate local thermal effects [16,17]. By topical application of photosensitizers and noninvasive NIR radiation, the thermal effects induced by PTT can be precisely controlled, thereby minimizing damage to non-targeted tissues [16,17]. The process can simultaneously destroy the cytoskeleton, inhibit biomolecule syntheses, damage tumor cell membranes, and ultimately cause tumor cell necrosis or apoptosis. Studies have shown that hyperthermic ablation of tumors can elicit an immune response, such as immunogenic cell death (ICD) [12–15]. Assisted by immune adjuvants, PTT could activate and redistribute immune effector cells, thus inducing robust antitumor immune responses [7,18]. R837, a typical immune adjuvant, can bind to Toll-like receptor 7 (TLR7) to promote the maturation of dendritic cells (DCs) by capturing tumor associated antigens and increase the secretion of pro-inflammatory cytokines [18–20]. As a result, DCs would undergo maturation, present tumor antigens to T cells, and activate effector T cells to respond to tumor cell-specific antigens. Finally, activated T cells would migrate to the tumor area, recognize and kill tumor cells, realizing powerful antitumor immunotherapy.

However, as a hallmark of the tumor, hypoxia has been reported to increase some immunosuppressive components, such as regulatory T cells (Tregs), related immunosuppressive cytokines, and tumor-associated macrophages (TAMs) [21–23]. TAMs are the most abundant immune cells in the TME, and are closely related to metastasis, angiogenesis and immunosuppression [24,25]. In general, they deviate from the classically activated M1-phenotype (pro-inflammatory, antitumor) and tend to polarize toward the alternatively activated M2-phenotype (anti-inflammatory, protumor) in hypoxic TME [24,26,27]. M2-TAMs can nourish tumor cells and promote angiogenesis in tumor tissues by secreting vascular endothelial growth factor (VEGF), and restrict adaptive immune responses by secreting cytokines such as interleukin 10 (IL-10) [26,28]. Therefore, hypoxia can significantly exacerbate the immunosuppressive TME and accelerate tumor progression and metastasis. Inarguably, the alleviation of hypoxia is essential for the implementation of immunotherapy, and efficient oxygen delivery could be the cure [21–23]. Among various oxygen delivery strategies, perfluorocarbon has been found to be an ideal platform for hypoxia attenuation. Since perfluorocarbon can not only effectively load oxygen at ambient temperature and pressure, but also readily release oxygen mimicking red cells' behavior, namely when encounters an externally low concentration of oxygen, the carried gas will be diffused responding the concentration gradient [21,29,30]. Moreover, it is non-toxic, thermally stable, and chemically inert.

Herein, we designed a nanoplatform that can relieve intratumoral hypoxia, reprogram the immunosuppressive microenvironment, and achieve photothermal-immunotherapy (Scheme 1). In this platform, perfluorooctyl bromide (PFOB, a type of perfluorocarbons), an advanced perfluorocarbon-based red blood cell substitute, is introduced and encapsulated in nanoplatform for oxygen delivery. IR780, a potent photosensitizer, is loaded into PFOB-based liposomes (designated as IR-R@LIP/PFOB) to achieve PTT. It has been reported that IR780 selectively accumulates in tumor tissues and retains preferentially in mitochondria, further enhancing the cytotoxicity of PTT [31–33]. Besides, IR780 can also act as a photoacoustic (PA)/fluorescence (FL) imaging contrast agent to monitor the distribution of these nanoplatforms and guide NIR laser irradiation [31,34]. Upon administration, NIR irradiation induces the photothermal conversion of IR780 to realize local ablation of the primary tumor. Then, a strong antitumor immune response can be expected by the PTT-triggered ICD effect; this effect is also strengthened by immune adjuvant R837. Following the hypoxia relief, TAMs tend to polarize from tumor-promoting M2-phenotype to tumoricidal M1-phenotype, and Tregs cells can be reduced especially in combination with anti-PD-1 antibody. The proliferation, activation, and infiltration of T cells can also be promoted. As a result, synergistic treatments of PTT and immunotherapy can be achieved. In addition, this synergy can not only suppress the growth of the primary tumor, but also further inhibit tumor recurrence and distant metastasis.

## 2. Experimental section

2.1. Materials

1,2-dipalmitoyl-sn-glycero-3-phosphatidylcholine (DPPC), 1,2-distearoyl-sn-glycero-3-phosphoethanolamine-N-[methoxy (polyethylene glycol)-2000] (DSPE-mPEG2000), and cholesterol were purchased from Xi'an Ruixi Biological Technology Co., Ltd (Xi'an, China). Imiquimod (R837) was purchased from Macklin Biochemical Co., Ltd (Shanghai, China). IR780 iodide and PFOB were purchased from Sigma-Aldrich (St. Louis, MO, USA). Trichloromethane ($CHCl_3$) and dimethyl sulfoxide (DMSO) were purchased from Chuandong Chemical Co. Ltd (Chongqing, China). 1,1′-dioctadecyl-3,3,3′,3′-tetramethylindocarbocyanine perchlorate (DiI), 2-(4-amidinophenyl)-6-indolecarbamidinedihydrochloride (DAPI), Mito-Tracker Green, adenosine triphosphate (ATP) assay kit, and mitochondrial membrane potential assay kit with JC-1 were purchased from Beyotime Technology (Shanghai, China). Cell Counting Kit-8 (CCK-8) was obtained from MedChemExpress (Shanghai, China). Calcein-AM and propidium iodide (PI) were purchased from Dojindo China Co., Ltd (Shanghai, China). Enzyme-linked immunosorbent assay (ELISA) kits including mouse interleukin-6 (IL-6), tumor necrosis factor-α (TNF-α), IL-10, IL-12, and interferon-γ (IFN-γ) were purchased from Meimian Industrial Co., Ltd (Jiangsu, China). Anti-high mobility group protein 1 (HMGB1) antibody and anti-calreticulin (CRT) antibody, Goat anti-rabbit IgG H&L (FITC) were purchased from Abcam (Shanghai, China). Anti-mouse PD-1 antibody (Anti-PD-1) was obtained from BioXcell (Lebanon, NH, USA). Fix&Perm Kit was purchased from Lianke Bio (China). *Roswell Park Memorial Institute* (RPMI)-1640 complete medium was purchased from Shanghai Zhong Qiao Xin Zhou Biotechnology Co., Ltd (China). Distilled water was obtained from a Millipore water system. All chemicals were of analytical grade and used without further purification.

2.2. Synthesis of IR-R@LIP/PFOB

IR-R@LIP/PFOB was synthesized by an emulsion strategy. Briefly, DPPC, DSPE-mPEG2000, cholesterol, IR780, and R837 (mass ratio 12: 4: 4: 1: 2) were dissolved in 10 mL of $CHCl_3$. The mixture was transferred to a round-bottom flask, and a thin film was formed after a rotary evaporation process in the dark (50 °C, 100 r min^{-1}). Distilled water (4 mL) was added to the flask and the lipid films were peeled with the help of bath sonication. Then, 0.4 mL of PFOB was added to the mixture and exposed to an ultrasonic probe (100 W, 2 min in total, 5 s on, 5 s off). Finally, the as-synthesized nanoplatforms were purified by centrifugation (6000 g, 3 min) for three times. IR@LIP/PFOB (without R837 loading) and R@LIP/PFOB (without IR780 loading) were synthesized according to the same procedure without the addition of the corresponding ingredients. IR-R@LIP (without PFOB loading) was prepared by extrusion through a polycarbonate film. Fluorescent dye DiI was added to the $CHCl_3$ mixture to obtain DiI-labeled nanoplatforms. To infuse oxygen in the PFOB core of the IR-R@LIP/PFOB, the nanoplatforms were placed in a pure oxygen-enclosed container overnight.

2.3. Characterization of IR-R@LIP/PFOB

The morphology of IR-R@LIP/PFOB was observed by a transmission electron microscopy (TEM, Hitachi 7500, Hitachi Ltd, Tokyo, Japan). The size distribution and zeta potential were measured by a dynamic light scattering (DLS) analyzer (Malvern Instruments, Malvern, UK). The absorption spectra of IR780 (dissolved in DMSO) and IR-R@LIP/PFOB were obtained using a SpectraMax M3 spectrophotometer (Molecular Devices, Sunnyvale, CA, USA). The R837 encapsulated in the nanoliposomes was
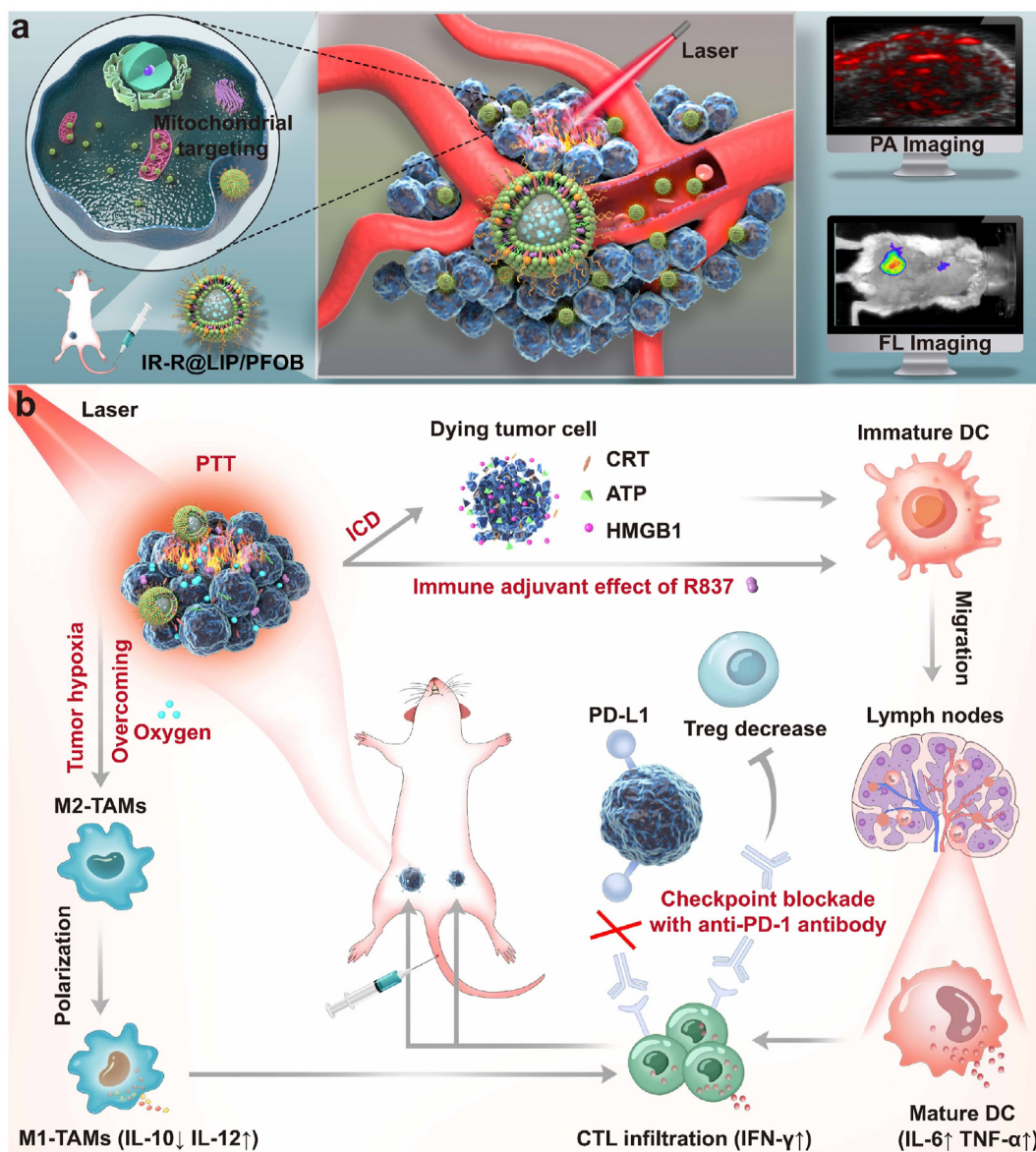
Scheme 1. (a) Schematic diagram of the PA/FL dual-modal imaging-guided NIR laser irradiation based on IR-R@LIP/PFOB with mitochondria-targeting capacity. (b) Schematic diagram illustrating the underlying mechanism of oxygen-carrying IR-R@LIP/PFOB-mediated photothermal-immunotherapy.

determined by high pressure liquid chromatograph (HPLC, Shimadzu, Tokyo, Japan). The encapsulation efficiency of IR780 and R837 were calculated according to the corresponding standard curve and the following equation:

Encapsulation efficiency (EE) = (weight of loaded IR780 or R837 in IR-R@LIP/PFOB/total weight of IR780/R837 added) × 100%

The oxygen-carrying capacity of PBS, IR-R@LIP, and IR-R@LIP/PFOB were tested by a portable dissolved oxygen meter (550 A, YSI, Ohio, USA). Briefly, IR-R@LIP and IR-R@LIP/PFOB pre-saturated with oxygen were added to anaerobic water, and the liquid surface was sealed with paraffin oil to isolate the air. Then, the oxygen concentration changes in anaerobic water under airtight conditions were measured by the dissolved oxygen meter. In addition, to evaluate the effect of PTT on oxygen-release profile of IR-R@LIP/PFOB, the IR-R@LIP/PFOB solutions were irradiated by an 808 nm laser (1.5 W cm^{-2}, 2 min) post 4 h storage in an anaerobic condition.

To evaluate the photothermal effects of IR-R@LIP/PFOB *in vitro*, different concentrations of IR-R@LIP/PFOB were added to 96-well plates and exposed to NIR laser (808 nm, 1.5 W cm^{-2}, 150 s). The infrared

thermal images and temperature changes were monitored by an infrared thermal imaging camera (Fotri226, Shanghai, China).

2.4. Cell culture and animal model

Murine breast cancer 4T1 cell lines were obtained from Procell Life Science & Technology Co., Ltd (Wuhan, China) and murine bone marrow-derived dendritic cells (BMDCs) were purchased from Otwo Biotechnology Co., Ltd (Shenzhen, China). Murine 4T1 cells and BMDCs were cultured in RPMI-1640 and *Dulbecco Modified Eagle Medium* (DMEM) complete medium, respectively. Cells were incubated at 37 °C with 5% CO$_2$.

All animal studies and procedures were conducted under a protocol approved by the Animal Ethics Committee of the First Affiliated Hospital of Chongqing Medical University. All animal experiments were conducted in accordance with the guidelines of the Chongqing Management Approach of Laboratory Animal. Female BALB/c mice (6–8 weeks) were purchased from the Experimental Animal Center of Chongqing Medical University. The unilateral 4T1 tumor-bearing mice models were

established by subcutaneous injection of 1×10^6 cells dispersed in 50 μL of serum-free medium into the mammary fat pad on the right side as the primary tumor. Four days later, the second tumor, as an artificial mimic of metastasis, was inoculated on the left mammary fat pad of the mice.

2.5. Assessment of intracellular uptake and mitochondria-targeting profile of IR-R@LIP/PFOB

The intracellular uptake of IR-R@LIP/PFOB by 4T1 cells was monitored by confocal laser scanning microscopy (CLSM, Nikon, Tokyo, Japan). Briefly, 4T1 cells were cultured in confocal-specific dishes at a density of 1×10^5 cells per well for 24 h. Then, medium containing DiI-labeled IR-R@LIP/PFOB or R@LIP/PFOB was added to dishes, respectively. After different incubation periods (0.5, 1, 2, 3, and 4 h), the cells were rinsed twice with phosphate buffer (PBS), and then fixed in 4% paraformaldehyde for 15 min. Ultimately, the cells were directly observed by CLSM after DAPI staining. Moreover, the FL intensity of DiI-labeled IR-R@LIP/PFOB and R@LIP/PFOB in 4T1 cells were quantitively analyzed by flow cytometry (BD FACSVantage SE, USA). To verify the mitochondrial targeting property of IR780, a certain amount of DiI-labeled IR-R@LIP/PFOB or R@LIP/PFOB (lipid concentration: 54.5 μg mL^{-1}) was incubated with 4T1 cells for 4 h, then washed twice with PBS. Afterward, Mito-Tracker Green was applied to label mitochondria. The mitochondrial localization of IR-R@LIP/PFOB or R@LIP/PFOB was visualized using CLSM.

2.6. Cytotoxicity of PTT, in vitro ICD, and in vitro DC maturation

To evaluate the *in vitro* cytotoxicity of PTT, 4T1 cells (5×10^3 cells per well) seeded in a 96-well plate were divided into 6 groups including: Control, Laser only, IR-R@LIP/PFOB, IR @LIP/PFOB + Laser, IR-R@LIP + Laser and IR-R@LIP/PFOB + Laser. The cells were co-incubated with different nanoliposomes (lipid concentration: 54.5 μg mL^{-1}) for 4 h. For laser irradiation groups, the cells were then exposed to 808 nm laser irradiation (1.5 W cm^{-2}, 2 min). Next, the cell viabilities of 4T1 cells were determined by the CCK-8 assay. To evaluate the PTT efficiency of IR-R@LIP/PFOB, cells maintained in confocal-specific dishes were subjected to the aforementioned treatments, and the live or dead cells were stained with Calcein-AM and PI, respectively. Finally, the cells were observed under CLSM. To test the changes of mitochondria membrane potentials, 4T1 cells in six groups were received corresponding treatments as aforementioned. After that, JC-1, a typical mitochondrial dye, was added to cells and cocultured for 20 min. The cells were rinsed with PBS, and harvested to detect the FL intensity of JC-1 monomers and JC-1 aggregates in cells by flow cytometry.

To study the ICD effect induced by PTT, the molecular signatures including CRT, HMGB1, and ATP were detected after various treatments as indicated. In detail, after the treatments, the anti-CRT antibody was added and incubated for 30 min. Then, the antibody was labeled by the goat anti-mouse IgG-FITC as a secondary antibody for CLSM observation. To detect the release of HMGB1, 4T1 cells were received same treatments with CRT measurement except that 4T1 cells were treated with cell permeates membrane solution (0.5%TritonX-100) before stained with anti-HMGB1. For ATP measurement, the content of ATP in cell supernatants was examined by the commercial ATP kit.

A Transwell system was used to evaluate *in vitro* DC maturation. Firstly, 4T1 cancer cells after different treatments (6 groups: Control, Laser only, IR-R@LIP/PFOB, IR@LIP/PFOB + Laser, IR-R@LIP + Laser, and IR-R@LIP/PFOB + Laser) were placed in the upper compartment of the transwell system, while BMDCs were seeded in the lower compartment. After 24 h of incubation, DCs were harvested and stained with anti-CD11c, anti-CD80 and anti-CD86 (CD11c-FITC: clone N418, REF. NO. 11-0114-82, eBioscience, CD80-APC: clone 16-10A1, REF. NO. 17-0801-82, eBioscience; CD86-PE: clone GL1, REF. NO. 12-0862-82, eBioscience). Finally, the DCs were analyzed by flow cytometry. The

proinflammatory cytokines including IL-6 and TNF-α from DCs suspension were determined by ELISA kits.

2.7. Biodistribution of IR-R@LIP/PFOB

Tumor accumulation and biodistribution of IR-R@LIP/PFOB in 4T1 tumor-bearing mice were tested by tracking the FL of IR780 with the *In Vivo Fluorescence Imaging System* (IndiGo 2.0.5.0, Berthold Technologies, Germany). To evaluate the biodistribution of IR-R@LIP/PFOB *in vivo*, 4T1 tumor-bearing mice were intravenously injected with IR-R@LIP/PFOB (lipid concentration: 5 mg mL^{-1}, 200 μL). The FL images were recorded at pre-set time points (0, 1, 3, 6, 24, and 48 h post injection), and the FL intensity was quantitatively analyzed by living image software. Organs of interest (tumor, heart, liver, spleen, lung, kidney) were dissected for *ex vivo* FL imaging to further detect the biodistribution of IR-R@LIP/PFOB.

PA imaging of IR-R@LIP/PFOB was conducted on Vevo LAZR Photoacoustic Imaging System (Visual Sonics Inc., Toronto, Canada). IR-R@LIP/PFOB suspension at different concentrations of IR780 (2, 4, 6, 8, and 10 μg mL^{-1}) was used for *in vitro* PA imaging, and the quantified PA signal intensities were analyzed by Vevo LAZR software. *In vivo* PA imaging was performed before and after (1, 3, 6, 24, and 48 h) intravenous injection of IR-R@LIP/PFOB (lipid concentration: 5 mg mL^{-1}, 200 μL), and the PA intensities within tumor regions were measured.

2.8. Evaluation of hypoxia status and polarization of TAMs

To evaluate the oxyhemoglobin saturation levels of tumors, 4T1 tumor-bearing mice were imaged by Vevo LAZR Photoacoustic Imaging System in oxyhemoglobin mode before and 24 h post injection of varied nanoliposomes (IR-R@LIP, R@LIP/PFOB, and IR-R@LIP/PFOB; 5 mg mL^{-1}, 200 μL). The oxygen saturation (sO$_2$ Avr Total) was analyzed by measuring the ratio between oxygenated hemoglobin ($\lambda = 850$ nm) and deoxygenated hemoglobin ($\lambda = 750$ nm). To examine hypoxia status in tumors, another eighteen 4T1 tumor-bearing mice were assigned into six groups as follows: (1) Control, (2) IR-R@LIP, (3) R@LIP/PFOB, (4) IR-R@LIP + Laser, (5) IR-R@LIP/PFOB and (6) IR-R@LIP/PFOB + Laser. The tumors in groups 4 and 6 were partially irradiated with 808 nm laser (1.5 W cm^{-2}) for 10 min at 24 h post the injection. Then, the mice in each group were sacrificed, and their tumor tissues were harvested and fixed in 4% paraformaldehyde for hypoxia inducible factor 1 (HIF-1α) immunofluorescence staining.

To evaluate the polarization state of TAMs, 4T1 tumor-bearing mice were randomly divided into six groups including (1) Control, (2) IR-R@LIP, (3) R@LIP/PFOB, (4) IR-R@LIP + Laser, (5) IR-R@LIP/PFOB and (6) IR-R@LIP/PFOB + Laser. The mice were intravenously injected with corresponding nanoliposomes (lipid concentration: 5 mg mL^{-1}, 200 μL). The tumors in groups 4 and 6 were partially irradiated with 808 nm laser (1.5 W cm^{-2}) for 10 min at 24 h post the injection. At 7 days post administration, the tumors were collected and homogenized for the preparation of single-cell suspension. M1 and M2-phenotype TAMs were distinguished by CD11b$^+$F4/80$^+$CD86$^+$ and CD11b$^+$F4/80$^+$CD206$^+$, respectively (PerCP-CY5.5-CD11b: clone M1/70, REF. NO. 45-0112-82, eBioscience; FITC-F4/80: clone BM8, REF. NO. 11-4801-82, eBioscience; APC-CD206: clone MR6F3, REF. NO. 17-2061-82, eBioscience). Cytokines including TNF-α and IL-6 in serum were also tested by ELISA kits.

2.9. In vivo immune response

For *in vivo* ICD assessment, 4T1 tumor-bearing mice were randomly divided into six groups, including Control, Laser only, IR-R@LIP/PFOB, IR@LIP/PFOB + Laser, IR-R@LIP + Laser and IR-R@LIP/PFOB + Laser. These mice were intravenously injected with corresponding nanoliposomes (lipid concentration: 5 mg mL^{-1}, 200 μL). At 24 h post

injection, mice in groups containing laser irradiation were exposed to an 808 nm laser (1.5 W cm^{-2}, 10 min). The temperature changes of the primary tumors during laser irradiation were recorded by an infrared thermal-imaging camera. Two days later, the tumor tissues were collected and sliced to detect the expression of CRT, HMGB1, and heat shock protein 70 (HSP70).

To investigate *in vivo* DC maturation rate, mice received the same treatments as the *in vivo* ICD experiments. At 3 days after the irradiation, tumor tissues, sentinel lymph nodes (SLN), and spleens were dissected for flow cytometry analysis after co-staining with CD11c-FITC, CD80-APC, and CD86-PE. In addition, the serum of mice was collected to measure the secretion levels of cytokines including TNF-α and IL-6.

To test the infiltration of T cells, bilateral 4T1 tumor-bearing mice were randomly divided into 7 groups (G1: Control, G2: IR-R@LIP/PFOB, G3: IR@LIP/PFOB + Laser, G4: IR-R@LIP + Laser, G5: IR@LIP/PFOB + Laser, G6: IR-R@LIP + Laser + anti-PD-1, G7: IR@LIP/PFOB + Laser + anti-PD-1, G refers to Group). Mice in G1 received saline only. Other mice were intravenous injected with the corresponding nanoliposomes (lipid concentration: 5 mg mL^{-1}, 200 μL). For groups containing laser irradiation, the primary tumors were exposed to 808 nm laser (1.5 W cm^{-2}, 10 min) at 24 h post injection. For G6 and G7, mice were intraperitoneally injected with anti-PD-1 (50 μg per mouse) at day 2, 4 and 6 (1, 3, and 5 days post laser irradiation). After 7 days of the irradiation, lymphocytes in distant tumor tissues and spleens were stained with corresponding fluorophore-conjugated antibodies. These stained cells were analyzed by flow cytometry to determine the infiltration of CD3$^+$CD8$^+$ T cells and CD3$^+$CD4$^+$Foxp3$^+$ T cells. Meanwhile, the section levels of IFN-γ were analyzed by the corresponding ELISA kit.

2.10. In vivo therapy experiments

To evaluate the effects of photothermal-immunotherapy *in vivo*, bilateral 4T1 tumor-bearing mice (n = 7) were randomly divided into seven groups (G1-G7) as described in section 2.9. For G6 and G7, mice were intraperitoneally injected with anti-PD-1 at the dose of 50 μg per mouse at 1, 3, 5, and 7 days post laser irradiation. The tumors on both sides and the body weights of each mouse were measured every other day after various treatments. The tumor volume was calculated as [length × (width)^2 × 0.5]. On the 3rd day and 20th day, one mouse from each group was sacrificed, respectively. Tumor tissues were collected and fixed in 4% paraformaldehyde. Then, the primary tumor tissues collected on the 3rd day were stained with hematoxylin and eosin (H&E) and terminal-deoxynucleotidyl transferase-mediated dUTP Nick-End labeling (TUNEL). The distant tumor tissues collected on the 20th day were stained with proliferating cell nuclear antigen (PCNA) to evaluate proliferation levels. The relative tumor volume (RTV) was calculated as follows:

$$RTV = V/V_0 \ (V = \text{tumor volume}, V_0 = \text{the original tumor volume}).$$

2.11. Biosafety assay of IR-R@LIP/PFOB

Healthy BALB/c mice (6–8 weeks) were randomly divided into five groups (Control, 3 days, 7 days, 14 days, and 30 days after intravenous injection, n = 5). Blood samples and major organs (heart, liver, spleen, lung, and kidney) were harvested on the 3rd, 7th, 14th or 30th day after intravenous administration of IR-R@LIP/PFOB (lipid concentration: 5 mg mL^{-1}, 200 μL). The blood samples were collected for routine blood examination and serum biochemical index tests, including liver functional markers (alanine aminotransferase, aspartate transaminase, total bilirubin), kidney functional markers (creatinine, urea nitrogen), myocardial enzyme spectrum (creatine kinase, and ʟ-lactate dehydrogenase). The major organs were stained with H&E for histological analysis.

2.12. Statistical analysis

All statistical analyses were performed with SPSS 26.0 software. Data were presented as mean ± standard deviation. The significance of the data is analyzed according to unpaired Student's t-test or one-way analysis of variance (ANOVA): ns (no significance), *$P < 0.05$, **$P < 0.01$, ***$P < 0.001$.

3. Results and discussion

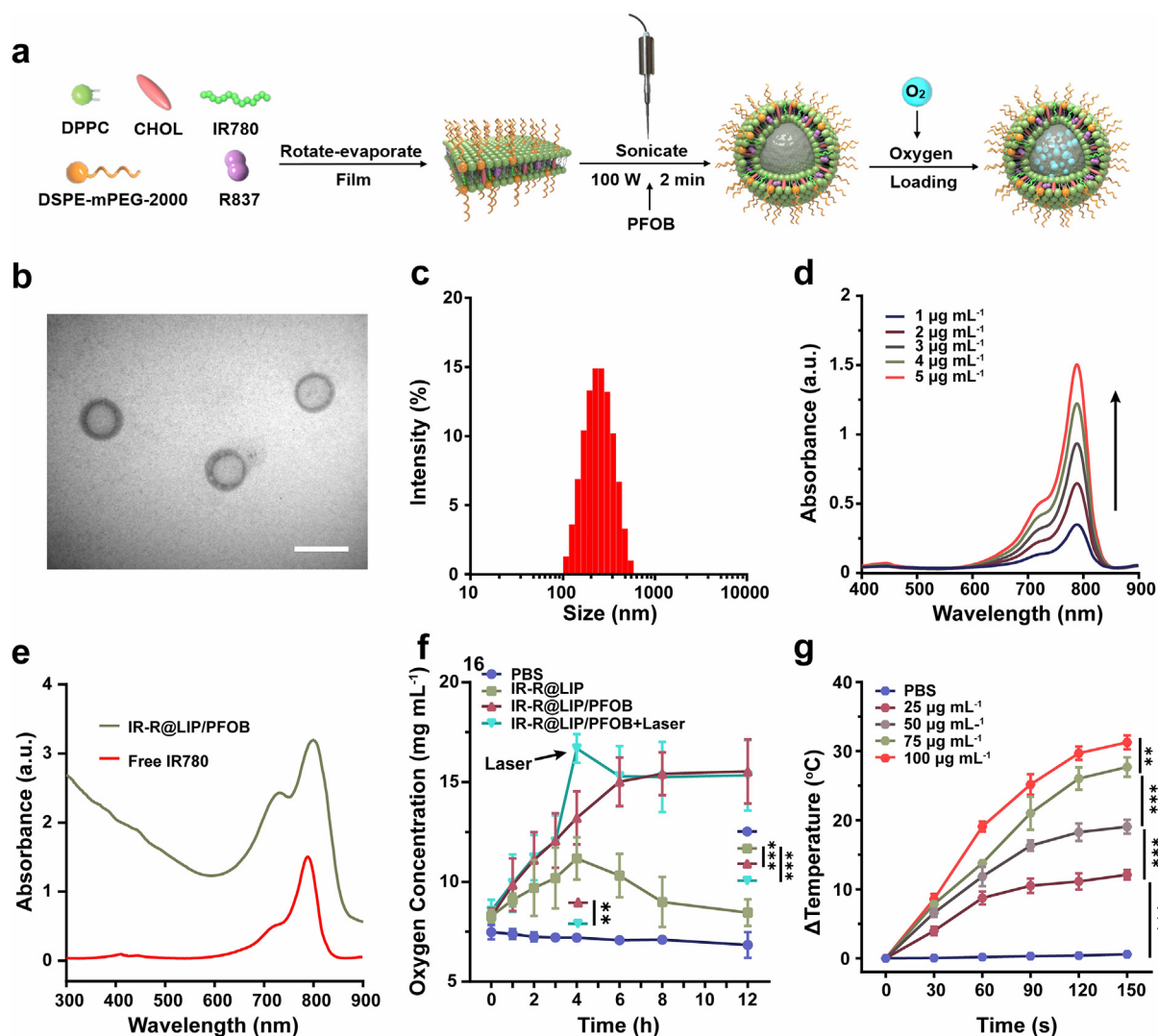### 3.1. Synthesis and characterization of IR-R@LIP/PFOB

IR-R@LIP/PFOB nanoplatforms were synthesized *via* rotation-emulsification, with lipophilic IR780 and R837 integrated into the lipid bilayer, and PFOB encapsulated in the core (Fig. 1a). The synthesized R@LIP/PFOB nanoliposomes were milky white, and turned dark green after the addition of IR780, indicating the successful loading of IR780 (Fig. S1a). TEM image showed that IR-R@LIP/PFOB were of spherical morphology with a core-shell structure (Fig. 1b and S1b). The average size of these nanoliposomes is around 210 nm as measured by DLS (Fig. 1c). The negative zeta potential of IR-R@LIP/PFOB might result from the presence of DSPE-mPEG2000, which was negatively charged [35]. The zeta potential of R@LIP/PFOB was further tested. It was found that the average zeta potentials of R@LIP/PFOB and IR-R@LIP/PFOB were −24.4 ± 0.7 mV and −19.5 ± 0.8 mV, respectively (Fig. S1c). This significant difference is consistent with the previous study demonstrating that the IR780 is a cationic molecule [36]. The absorbances of IR780 in IR-R@LIP/PFOB were characterized by UV–Vis spectra. It was found that IR780 exhibited a characteristic absorption peak at λ = 788 nm, the absorbance of which showed a concentration-dependent manner (Fig. 1d). IR-R@LIP/PFOB showed similar characteristic absorption of free IR780, indicating the successful loading of IR780 (Fig. 1e). The successful encapsulation of R837 was further demonstrated by HPLC determination (Fig. S2). Moreover, according to the standard curves (Fig. S3), the encapsulation efficiency of IR780 and R837 in IR-R@LIP/PFOB were calculated to be 73.4 ± 2.3% and 65.7 ± 4.1%, respectively.

Previous studies demonstrated that PFOB, a model perfluorocarbons compound, possesses the capacity of oxygen delivery [37–39]. The carried oxygen can be released by responding to an oxygen concentration gradient in an anoxic environment. To demonstrate the response, an *in vitro* oxygen release assay was performed in an anaerobic environment. As shown in Fig. 1f, after adding oxygen-saturated IR-R@LIP/PFOB into anaerobic water, the dissolved oxygen concentration in the solution rose from 8.3 to 15.5 mg mL^{-1}. Besides, it was found that photothermal effect triggered by NIR laser irradiation could promote O$_2$ release from PFOB. In comparison, in the absence of PFOB, oxygen in IR-R@LIP suspension (pre-saturated with oxygen) would rapidly disperse into anaerobic water, resulting in a slight increase in oxygen concentration. Although paraffin covers prevent exchange with the air, oxygen in the system slowly released into the air, resulting in a decrease in oxygen concentration. PBS without oxygen loading could not elevate the oxygen concentration of the system. The results indicated that the loading of PFOB in the IR-R@LIP/PFOB would be an excellent strategy for oxygen delivery.

To examine the photothermal capacity of IR-R@LIP/PFOB, the temperature changes of IR-R@LIP/PFOB at different concentrations after 808 nm laser irradiation were recorded using a thermal infrared camera (Fig. 1g, Fig. S4). According to the quantitative analyses, the temperature of IR-R@LIP/PFOB under laser irradiation (1.5 W cm^{-2}) presented a concentration-dependent manner, with highest temperature increase (△T = 31.3 °C) at 100 μg mL^{-1} of IR780 within 150 s. Comparatively, the PBS did not show any temperature elevation. The results demonstrated that IR-R@LIP/PFOB has an excellent photothermal capacity and could potentially act as a photothermal regent for tumor hyperthermia.

3.2. Exploration of the immunogenic cell killing capacity assisted by IR-R@LIP/PFOB

To achieve accurate targeted therapy and improve the efficacy of

Fig. 1. Characterizations of IR-R@LIP/PFOB. (a) Schematic illustration of the synthesis of IR-R@LIP/PFOB. (b) Representative TEM image of IR-R@LIP/PFOB (scale bar = 200 nm). (c) Size distribution of IR-R@LIP/PFOB as measured by DLS. (d) UV–vis absorbance spectra of IR780 at different concentrations. (e) UV–Vis spectra of IR780 and IR-R@LIP/PFOB. (f) Dissolved oxygen profiles of IR-R@LIP/PFOB when in anaerobic water (n = 3). (g) *In vitro* temperature changes of IR-R@LIP/PFOB at different concentrations under laser irradiation (n = 3, 1.5 W cm^{-2}).

photothermal-immunotherapy, efficient tumor accumulation and cellular uptake of therapeutic agents are the important prerequisites. Therefore, we first evaluate the cellular uptake of IR-R@LIP/PFOB. IR-R@LIP/PFOB were co-incubated with 4T1 cells for different time durations (0.5, 1, 2, 3, and 4 h), and cells were then analyzed by CLSM and flow cytometry. As shown in Fig. 2a, while the red FL increased with a prolonged incubation time in the cells treated both with IR-R@LIP/PFOB and R@LIP/PFOB, much stronger FL was observed in IR-R@LIP/PFOB-treated group compared with those incubated with R@LIP/PFOB, which could be ascribed to the IR780-promoted cellular uptake/aggregation. Quantitative analyses by flow cytometry also showed that IR-R@LIP/PFOB exhibited significantly enhanced cellular uptake in contrast with R@LIP/PFOB (Fig. 2b and c).

In addition to preferable aggregation in tumor cells, it has been reported that IR780 also exhibits the ability to target mitochondria of tumor cells, which can further improve the efficiency of PTT [31–33,40]. To verify the mitochondrial targeting ability of IR780, 4T1 cells were co-incubated with IR-R@LIP/PFOB or R@LIP/PFOB nanoliposomes for 4 h. Cells were then stained with Mito-tracker and observed by CLSM. The results (Fig. 2d and Fig. S5) showed that the red FL of IR-R@LIP/PFOB was found in mitochondria, while negligible FL was

observed in cells treated with R@LIP/PFOB (without IR780). The yellow FL in merged images suggested the excellent colocalization of IR-R@LIP/PFOB and mitochondrial, while only a low percentage of colocalized R@LIP/PFOB signal with mitochondrial was detected. The result verified the outstanding mitochondrial targeting ability of IR780. Taking into account the hyperpyrexia susceptibility of mitochondria, the mitochondria-targeting capacity of IR-R@LIP/PFOB would be likely to enhance the therapeutic efficacy of PTT.

After verifying the accurate mitochondrial targeting and excellent high thermal efficiency of IR-R@LIP/PFOB, *in vitro* photothermal cytotoxicity was then evaluated by the standard CCK-8 assay. As depicted in Fig. 2e, the PTT treated-groups (IR@LIP/PFOB + Laser, IR-R@LIP + Laser and IR-R@LIP/PFOB + Laser) showed an obvious killing effect on tumor cells, while the sole addition of PFOB and R837 had only little therapeutic effect, as these two components did not result in temperature rise. The photothermal cytotoxicity of IR-R@LIP/PFOB was visualized *via* live/dead cell staining observed by CLSM (Fig. 2f). The confocal images showed massive red FL in PTT treated-groups, while no/negligible red FL was observed in other groups. JC-1, a reliable mitochondrial membrane potential probe, was further used to detect the changes of mitochondrial membrane potential of 4T1 cells post various treatments *via* flow
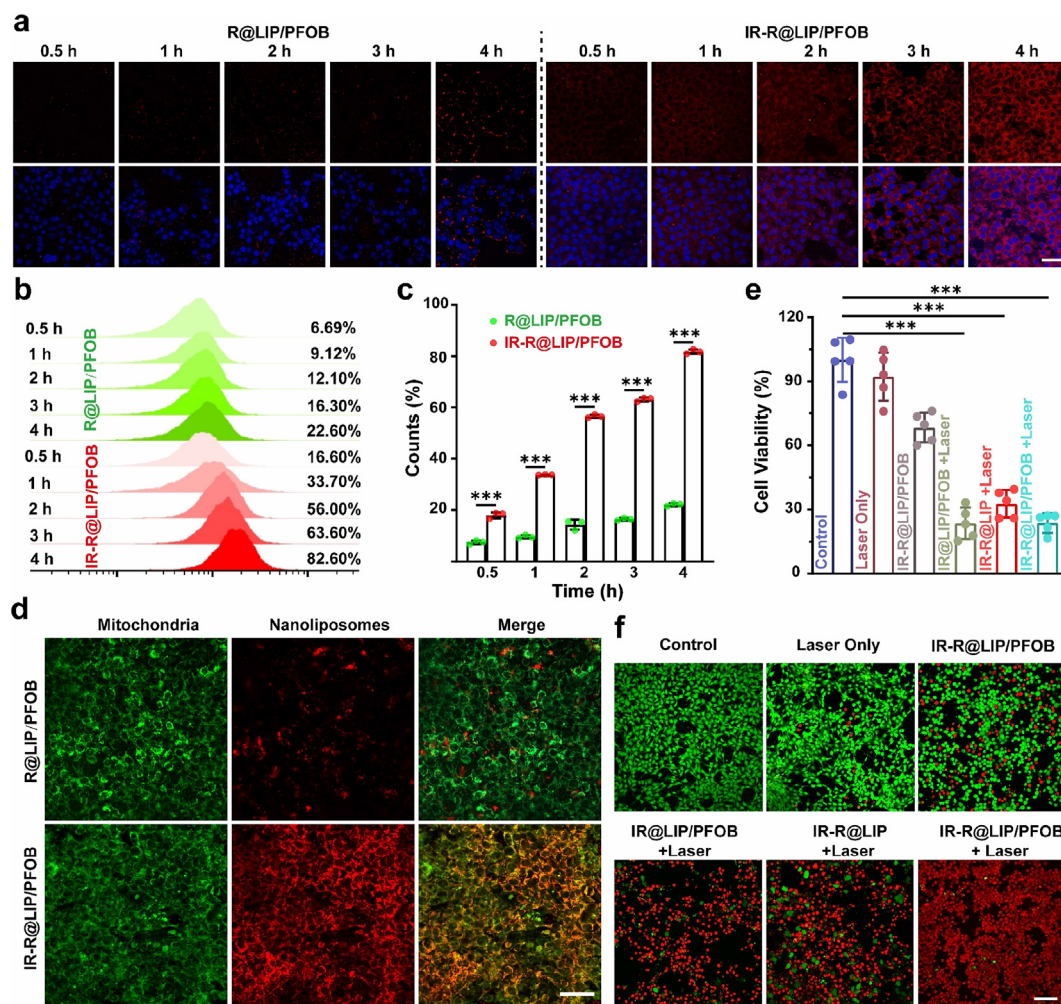
Fig. 2. Intracellular uptake and cytotoxicity. (a–c) Intracellular uptake of R@LIP/PFOB and IR-R@LIP/PFOB nanoliposomes (labeled with DiI) detected by CLSM (scale bars = 25 μm) and flow cytometry after various intervals of coincubation (n = 3, ***$P < 0.001$). (d) Mitochondrial location of R@LIP/PFOB and IR-R@LIP/PFOB nanoliposomes (labeled with DiI) as monitored by Mito-Tracker (scale bar = 50 μm). (e) CCK-8 results after various treatments. (n = 5, ***$P < 0.001$). (f) CLSM images of 4T1 cells stained by Calcein AM/PI after different treatments (scale bar = 100 μm).

cytometry. By determining the fluorescence of JC-1 aggregates and JC-1 monomers, representing high and low mitochondrial membrane potential respectively, it was found that 4T1 cells post JC-1 staining exhibited remarkably reduced mitochondrial membrane potential upon being co-cultured with IR780-loaded nanoliposomes in the presence of laser irradiation (Fig. S6). On the contrary, plain laser irradiation exhibited negligible disturbance on the change of mitochondrial membrane potential. These results demonstrated that IR-R@LIP/PFOB-based PTT is able to induce mitochondrial dysfunction. Therefore, it can be concluded that IR780-based nanoplatforms (IR@LIP/PFOB, IR-R@LIP and IR-R@LIP/PFOB) combined with laser irradiation can trigger a potent PTT effect towards tumor cells.

PTT has been reported to be accompanied by the release of diverse damage-associated molecular patterns (DAMPs), including the exposure of CRT, and the release of HMGB1 and ATP [15,41,42]. Therefore, the potential immunostimulatory efficacy of PTT assisted by IR-R@LIP/PFOB was evaluated next. From the CLSM observation (Fig. 3a), it was found that treatments with PTT including IR@LIP/PFOB + Laser, IR-R@LIP + Laser and IR-R@LIP/PFOB + Laser, led to the most effective expression of CRT on plasma membrane and release of HMGB1 (Fig. S7). In marked contrast, the Laser-only and IR-R@LIP/PFOB-only groups showed minimal influence on the presence of CRT and the release of HMGB1. Additionally, we found that 4T1 cells treated by PTT (IR@LIP/PFOB + Laser, IR-R@LIP + Laser, IR-R@LIP/PFOB + Laser)

resulted in the most effective ATP release, while no detectable ATP was observed in other control groups (PBS, Laser only, IR-R@LIP/PFOB) (Fig. 3b). Having known that CRT, HMGB1 and ATP are typical markers of ICD, the above results collectively validated that PTT could elicit effective ICD of tumor cells.

As a critical messenger in priming immunity signals, DAMPs work as a biological indicator to trigger DC maturation by phagocytizing dead or dying tumor cells [43,44]. By utilizing BMDCs as the model, we estimated the IR-R@LIP/PFOB-based PTT-immune system for effective stimulation of DCs. Tumor cells after different treatments were co-incubated with BMDCs, and the proportion of DC maturation was determined by flow cytometry (Fig. 3c and d). As a result, we found that both IR-R@LIP + Laser and IR-R@LIP/PFOB + Laser groups could significantly boost the maturation of BMDCs as indicated by the increased proportion of CD80+CD86+ on DCs (44.4 ± 3.5% and 47.6 ± 0.7%, respectively). However, only ICD alone or the immune adjuvant-only group (IR@LIP/PFOB + Laser, IR-R@LIP/PFOB) showed only moderate effects on the maturation of BMDCs with CD80+CD86+ ratio at 35.7 ± 2.6% and 37.1 ± 2.9%, respectively. Additionally, DCs upon maturation will secrete a variety of proinflammatory cytokines, which are considered as representative hallmarks of immune responses [45]. It was uncovered that the treatment of PTT combined with immune adjuvant R837 could lead to the secretion of cytotoxic cytokines of TNF-α and IL-6 (77.2 ± 1.2 ng mL^{-1} and 42.3 ± 3.6 pg mL^{-1}, respectively), the
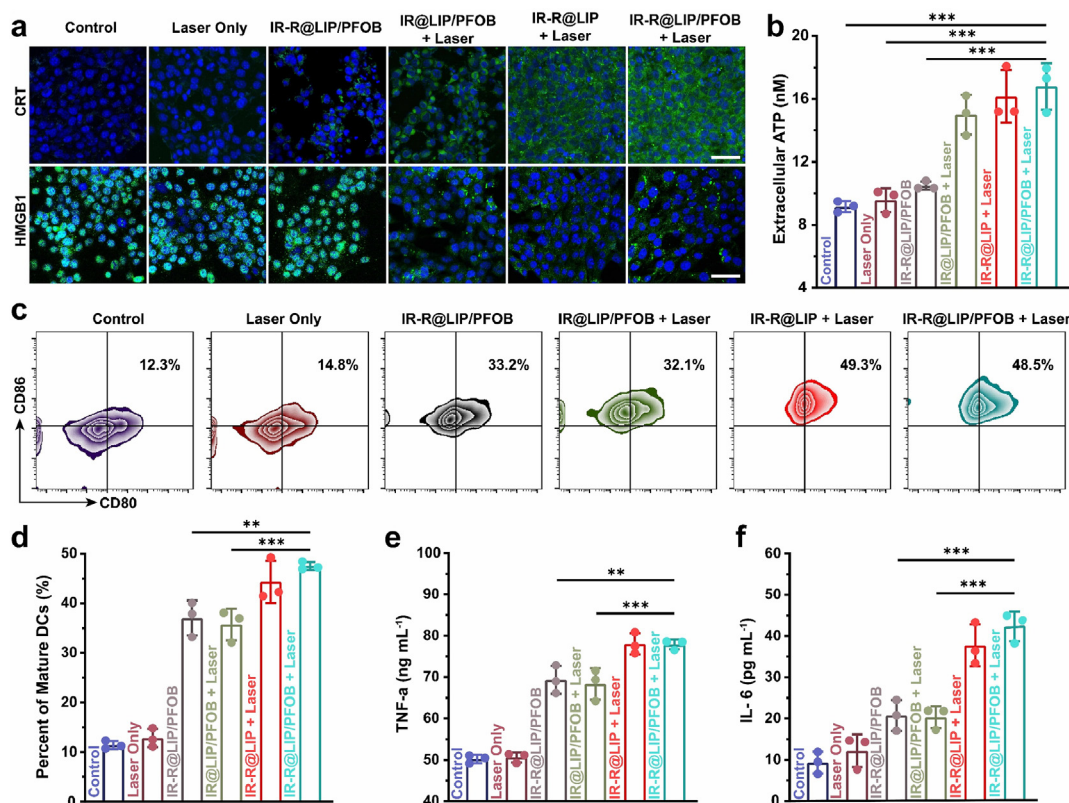
Fig. 3. *In vitro* **ICD and DCs maturation.** (a) CLSM images of CRT and HMGB1 exposure of 4T1 cells after various treatments (scale bars = 50 μm). (b) ATP in 4T1 suspensions after various treatments as detected by the ATP kit. (n = 3, ***$P < 0.001$). (c–d) The proportion of mature DCs (CD11c$^+$CD80$^+$CD86$^+$) as detected by flow cytometry after different treatments (n = 3, **$P < 0.01$, ***$P < 0.001$). (e–f) Cytokine levels of TNF-α and IL-6 in DC suspensions were detected by the corresponding ELISA kits (n = 3, **$P < 0.01$, ***$P < 0.001$).

level of which were higher than that those cells received with only IR-R@LIP/PFOB stimulation (69.3 ± 3.8 ng mL^{-1} and 20.7 ± 3.7 pg mL^{-1}, respectively) or IR@LIP/PFOB + Laser (68.4 ± 3.8 ng mL^{-1} and 20.3 ± 2.7 pg mL^{-1}, respectively) (Fig. 3e and f). These results revealed that IR-R@LIP/PFOB combined with laser irradiation strengthened the immunity activation, and the combined treatments could achieve synergistic therapeutic effects.

3.3. Biodistribution of IR-R@LIP/PFOB

The efficient accumulation of IR-R@LIP/PFOB in tumor sites is highly desirable for subsequent *in vivo* PTT and immunotherapy, thus monitoring the biodistribution of IR-R@LIP/PFOB *via* real-time imaging technology is necessary. PA holds great potential for clinical translation due to the sufficient imaging depth and high sensitivity. IR780 has been widely demonstrated as a PA imaging contrast agent [31,34,46]. As a near-infrared dye, IR780 is also recognized as an excellent FL contrast agent, so tumor accumulation and biodistribution of IR-R@LIP/PFOB in 4T1-tumor-bearing mice can be tracked by FL/PA dual imaging [31,34, 46]. *In vivo* FL imaging of tumor-bearing mice was conducted after the intravenous administration of IR-R@LIP/PFOB. As shown in Figs. S8a and S8b, significantly enhanced FL signals were detected within tumors with prolonged circulation time, and peaked at 24 h post injection. Tumor tissues and main organs of mice were collected for *ex vivo* imaging to compare the FL intensities (Figs. S8c and S8d), and the FL signal of tumors were stronger than that of other major organs, indicating the preferable enrichment of IR-R@LIP/PFOB towards tumors. As shown in Fig. S8e, PA intensities of IR-R@LIP/PFOB showed a concentration-dependent manner, demonstrating the feasibility of IR-R@LIP/PFOB to enhance PA imaging. *In vivo* PA imaging was further performed to detect the aggregation of IR-R@LIP/PFOB in tumor tissues.

It was observed that PA signal in the tumor area gradually increased after administration, and peaked at 24 h post injection, which was consistent with *in vivo* FL imaging results (Figs. S8f and S8g).

3.4. Evaluation of hypoxia status and the polarization of TAMs

Encouraged by the efficient oxygen-carrying capability of PFOB, we then systemically evaluated their potency in relieving tumor hypoxia. The oxygenated hemoglobin level was measured using PA imaging in oxyhemoglobin mode. It was found that mice received IR-R@LIP/PFOB administration showed obvious increase of oxygenated hemoglobin signals, suggesting the increased oxygen content within tumors (Fig. 4a). However, in the absence of IR780, the PA signal in R@LIP/PFOB group was weaker than that of the IR-R@LIP/PFOB group, indicating the critical role of IR780 in guiding IR-R@LIP/PFOB accumulation in tumors. In sharp contrast, mice treated by IR-R@LIP showed negligible PA signal. The quantitative analysis showed that after 24 h of injection, the tumor oxygenation of IR-R@LIP/PFOB group increased significantly from an average sO$_2$ of 3.2 ± 0.3% to 13.6 ± 0.4%, and that of R@LIP/PFOB group also increased from an average of 2.9 ± 0.1% to 6.0 ± 0.5%, while the tumor oxygenation of the control group and IR-R@LIP was almost unchanged (Fig. 4b). Moreover, to evaluate the effects of PFOB-loaded nanoliposomes and PTT on hypoxia TME, another six groups of mice with 4T1 tumors were treated as below: (1) Control, (2) IR-R@LIP, (3) R@LIP/PFOB, (4) IR-R@LIP + Laser, (5) IR-R@LIP/PFOB and (6) IR-R@LIP/PFOB + Laser. The tumors in groups 4 and 6 were partially irradiated with laser. At 24 h post aforementioned treatments, mice were sacrificed with their tumors harvest for immunofluorescence staining. By evaluating the expression of hypoxia HIF-1α, which is a typical indicator of hypoxia [47,48], it was found that the tumor slices collected from the mice with IR-R@LIP/PFOB + Laser treatment exhibited the significantly
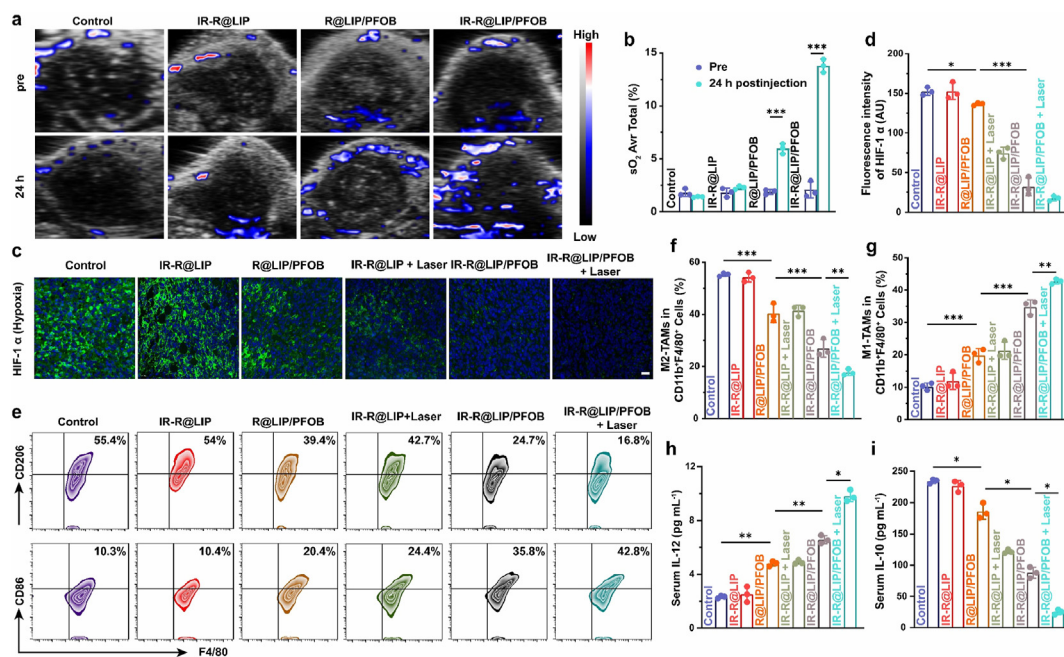
Fig. 4. Evaluation of tumor hypoxia and the immune response *in vivo*. (a–b) Representative PA images of 4T1 tumors treated with various agents in oxyhemoglobin mode and the corresponding quantitative analysis of oxyhemoglobin saturation within tumor sites (n = 3). (c–d) Immunofluorescent images of tumor slices stained by the hypoxia probe HIF-1α (scale bars = 20 μm) and the corresponding quantitative analysis. (e–g) Representative flow cytometry plots and corresponding quantitative analysis of tumoral macrophages in different groups (M2-TAMs gated on CD206$^+$, M1-TAMs gated on CD86$^+$) in CD11b$^+$F4/80$^+$ cells in tumors after various treatments (n = 3, *$P < 0.05$, **$P < 0.01$, ***$P < 0.001$). (h–i) Cytokine levels of IL-12 and IL-10 in serum post various treatments (n = 3, *$P < 0.05$, **$P < 0.01$).

reduced expression of HIF-1α. In contrast, treatment with injection of IR-R@LIP/PFOB or PTT alone led to moderately reduced expression of HIF-1α, while plain IR-R@LIP without PFOB loading negligibly disturbed the expression of HIF-1α (Fig. 4c and d).

As tumor hypoxia is a driving force in immunosuppressive TME [21–23,49], the potency of IR-R@LIP/PFOB in reversing the immunosuppressive state was then evaluated. After that, we carefully investigated the influence of IR-R@LIP/PFOB in combination with PTT treatment on the differentiation of TAMs polarization within tumors. To this end, six groups of mice with 4T1 tumors received corresponding treatments as mentioned above. At 7 days post-treatments, mice in each group were sacrificed, and their tumors were harvested for flow cytometry analysis. Consistent with their significant capacity to attenuate tumor hypoxia, the treatment with IR-R@LIP/PFOB exhibited moderate polarizing effect on M2-TAMs (CD11b$^+$F4/80$^+$CD80$^+$) in tumors (Fig. 4e and f). In combination with PTT, the polarizing effect of TAMs was further enhanced, with 42.7 ± 0.8% of M1-TAMs and 17.8 ± 1.0% of M2-TAMs in tumors. Additionally, the PTT alone slightly promoted the TAMs polarization with 21.3 ± 2.7% of M1-TAMs and 41.4 ± 2.2% of M2-TAMs in tumors. Of note, in addition to PTT-induced hypoxia attenuation, the mechanism of PTT to promote TAMs polarization has not been understood yet. In a recent study by *Li* et al., it reported that PTT could mediate inactivation of respiration chain oxidase, and which consequently induced phenotypic change of macrophages [50]. Studies have shown that M1-phenotype TAMs can kill tumor cells by producing inflammatory cytokines, activating effector T cells, and promoting apoptosis [51,52]. To further assess the polarization of TAMs, the serum of above-treated mice was taken to detect the two characteristic cytokines of M1 and M2-phenotype TAMs (IL-12 and IL-10, respectively). It was found that the treatment with IR-R@LIP/PFOB-based PPT could significantly increase the secretion of IL-12 (Fig. 4h), while reducing the secretion of IL-10 (Fig. 4i). Collectively, these results demonstrate that the combinational treatment (PTT and IR-R@LIP/PFOB) is effective in modulating hypoxia TME, and further promoting the polariton of M2-TAMs.

3.5. In vivo immune response

Encouraged by the *in vitro* results, *in vivo* immune response was further evaluated. First, we tested the potential immunostimulatory efficacy of such photothermal-immunotherapy strategy by evaluating the capability to induce ICD *in vivo*. According to the FL/PA imaging, IR-R@LIP/PFOB nanoplatforms can efficiently accumulate in tumors and peaked at 24 h post injection. Therefore, the tumors were irradiated with an NIR laser (808 nm, 1.5 W cm^{-2}, 10 min) at 24 h post injection. The thermal images of mice were acquired by an infrared thermal imaging camera (Fig. S9a). It can be seen that the temperature within tumor regions of mice treated by IR-R@LIP/PFOB + Laser rapidly reached higher than 50 °C (Fig. S9b), which was sufficient to initiate the ablation of tumor cells. After that, the tumor tissues were collected for immunofluorescence staining to detect the expression of CRT, HMGB1 and HSP70. As shown by the immunofluorescence images (Fig. 5a), the tumors that received IR-R@LIP/PFOB + Laser treatment experienced the most serious cellular stress, resulting in the exposure of CRT and the release of HMGB1 and HSP70. These results provided compelling evidences that PTT not only induced local tumor ablation, but also exhibited a systemically immunostimulatory effect.

Upon CRT exposure, immature DCs phagocytize the antigens and subsequently process these antigens into peptides as they migrate to nearby lymph nodes and undergo maturation [53]. Based on the *in vitro* experimental result, we have demonstrated that IR-R@LIP/PFOB + Laser could induce the maturation of DCs. To further investigate the DC maturation level *in vivo*, 3 days after the indicated treatments, the tumor tissues were harvested to prepare tumor single-cell suspension and stained with CD11c, CD80, and CD86. As shown in Fig. 5b and c, the integration of R837 evidently endowed PTT (IR@LIP/PFOB + Laser) with a stronger capability to facilitate DC maturation. Specifically, IR-R@LIP/PFOB + Laser induced the highest level of DC maturation in tumors (25.6 ± 1.0%), which outperformed PTT alone (12.0 ± 0.8%) and IR-R@LIP/PFOB (15.6 ± 2.0%). Not only can these nanoplatforms stimulate the maturation of DCs, but also can lead to systemic immune
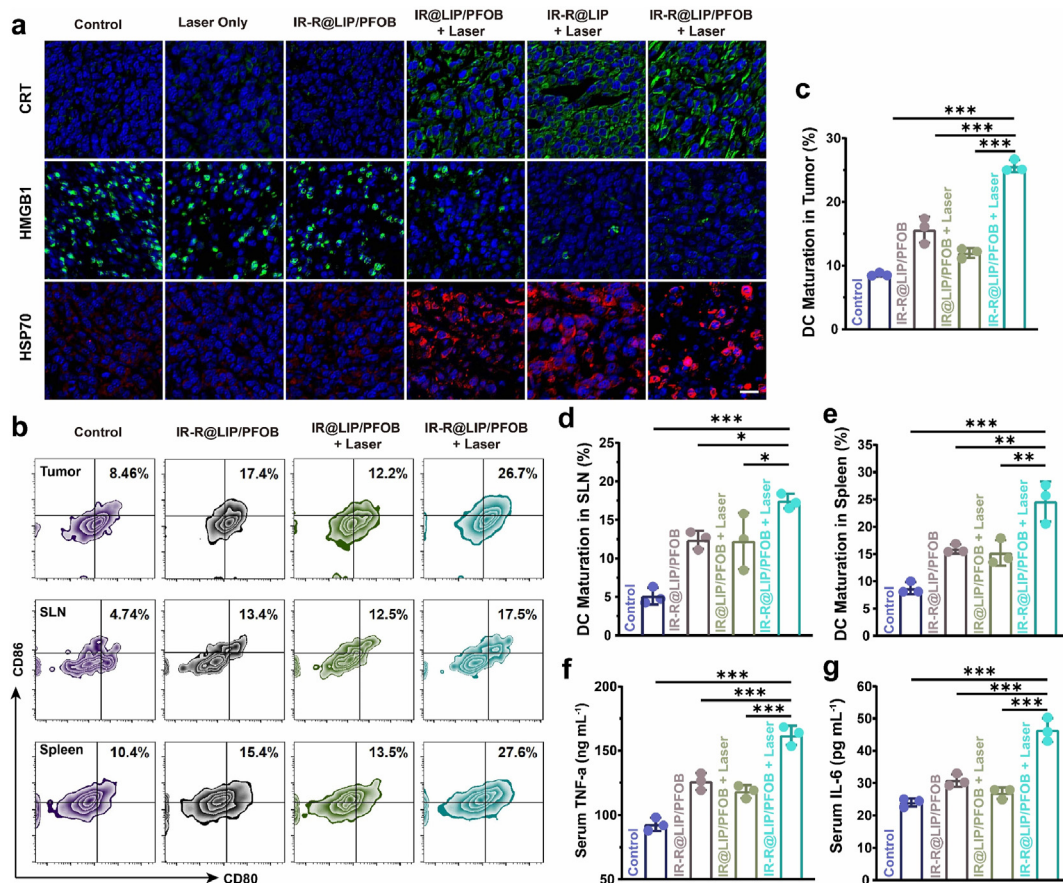
Fig. 5. The potency of IR-R@LIP/PFOB + Laser to introduce ICD and promote DC maturation *in vivo*. (a) Immunofluorescent images of tumor slices stained by CRT, HMGB1, and HSP70 (scale bar = 20 μm). (b–e) Representative flow cytometry plots of DCs in tumors, SLN, and spleen post various treatments (n = 3, *$P < 0.05$, **$P < 0.01$, ***$P < 0.001$). (f–g) Cytokine levels of TNF-α and IL-6 in serum detected by ELISA kits (n = 3, ***$P < 0.001$).

activation. Consistent with the observation in tumors, the percentages of matured DCs in SLN and spleens were remarkably enhanced after the combination of PTT and R837 (Fig. 5b, 5d-e). During DC maturation, a variety of cytokines could be released. Thus, to further elucidate the immune response, two characteristic cytokines of TNF-α and IL-6 were assessed using ELISA kits (Fig. 5f and g). The combination of PTT and immune-adjuvant R837 showed the highest serum TNF-α and IL-6 content, and the difference was statistically significant compared with other groups. In detail, the secretion of TNF-α and IL-6 in IR-R@LIP/PFOB + Laser-treated group were nearly doubled in control group. These results indicate that PTT combined with R837 can be used as an effective immune stimulator for subsequent cancer immunotherapy.

Upon DC maturation, major histocompatibility complex (MCH)-TAAs could be presented to native T cells, which can be activated and then redistribute *in vivo* [54]. To validate this hypothesis, we subsequently implanted mice with bilateral 4T1 tumors, and then injected various nanoplatforms together with laser irradiation on the primary tumors. Next, the infiltration of T cells in distant tumor tissues and spleens were evaluated by flow cytometry. As shown in Fig. 6a-c, in both tumors and spleens, the mice treated with IR-R@LIP/PFOB + Laser + anti-PD-1 (G7) demonstrated the highest proportion of CD3⁺CD8⁺ T cells, and with the lowest percentage of immunosuppressive Treg cells (CD3⁺CD4⁺Foxp3⁺) (Fig. 6d and e, S10). It is worth noting that bare IR-R@LIP/PFOB (G2) could also inhibit the percentage of Treg, which probably resulted from the relieved hypoxia status. Indeed, PFOB and anti-PD-1 both contributed to the infiltration of T cells and suppressed immunosuppressive Treg cells. Furthermore, it was also found that IR-R@LIP/PFOB + Laser + anti-PD-1 lead to a potent section of IFN-γ (Fig. 6f). Together with the TAMs polarization observation, these results collectively showed the

proposed therapeutic strategy (IR-R@LIP/PFOB + Laser + anti-PD-1 (G7)) can significantly promote the infiltration of M1-TAMs and cyto-toxic CD3⁺CD8⁺ T cells, while suppress the frequency of immunosuppressive M2-TAMs and Tregs. The significant *in vivo* immune response could be attributed to IR-R@LIP/PFOB-mediated tumor hypoxia attenuation, PTT-induced ICD, immune-adjuvant R837-promoted DC maturation, as well as immune checkpoint blockade.

3.6. In vivo tumor inhibition study

The intriguing *in vitro* therapeutic efficacy and powerful immune response mediated by IR-R@LIP/PFOB seemingly merit its effective *in vivo* therapeutic outcome. It is also expected that this approach can be effective against not only the primary tumor, but also metastasis. In this regard, mice with bilateral tumors were employed and randomly divided into 7 groups and received the corresponding treatments as illustrated in Fig. 7a. By monitoring the volume of primary tumors, it was found that IR-R@LIP/PFOB-treated group showed slight inhibitory effect on tumor growth (Fig. 7b). Comparatively, IR@LIP/PFOB + Laser and IR-R@LIP + Laser could significantly suppress the growth of tumors at the early stage, but then the tumors recurred and gradually grew after a few days, indicating that the tumors could not be completely inhibited by using PTT only. The primary tumors in G5-7 were completely suppressed, and no tumor recurrence was found, indicating a strong therapeutic effect of these treatments, which can be assigned to PFOB-mediated immunosuppressive microenvironment alleviating, or R837-assisted DC maturation, or/and anti-PD-1-mediated immune checkpoint blockade. In addition, we found that IR-R@LIP/PFOB + Laser and IR-R@LIP + Laser + anti-PD-1-treated groups showed moderate inhibition efficacy to
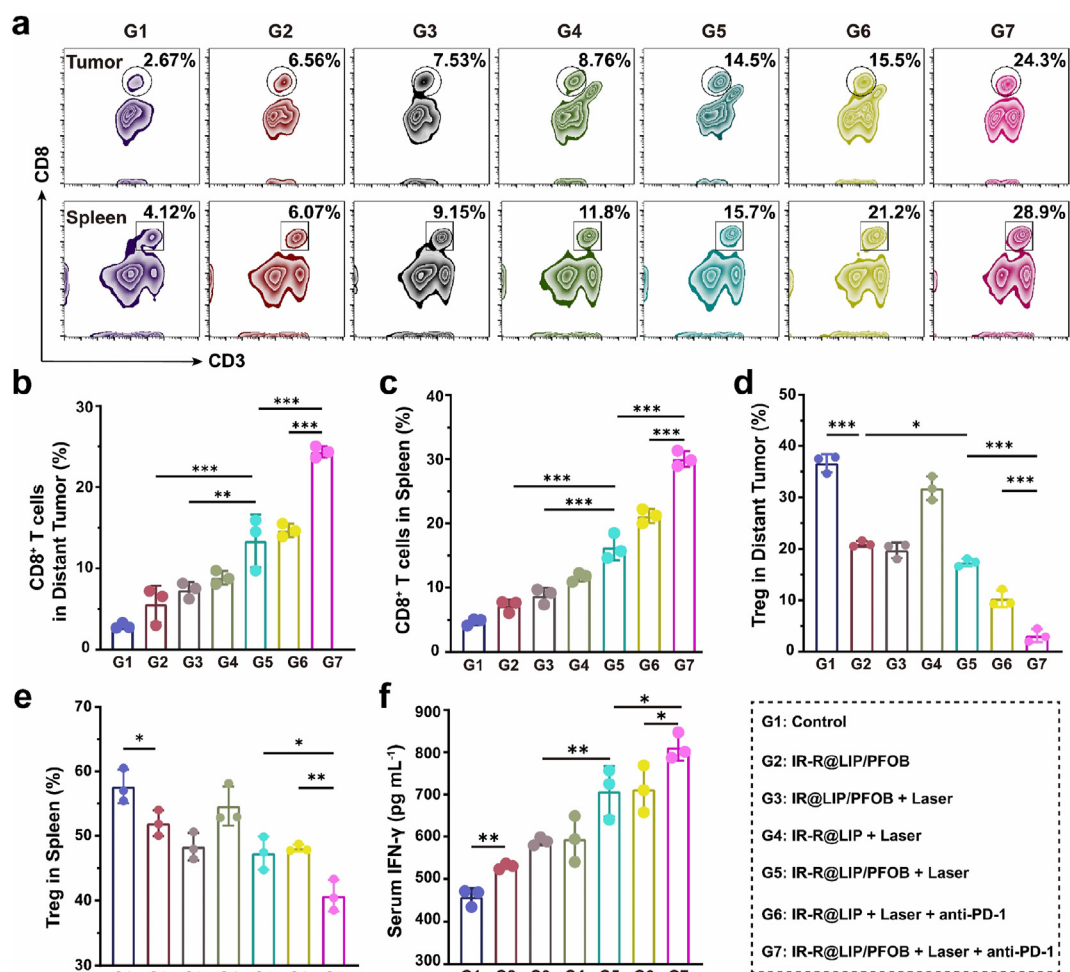
Fig. 6. Infiltration of T cells and Treg cells. (a–c) Flow cytometry analysis of CD8$^+$ T cells (CD3$^+$CD8$^+$) infiltration in distant tumors and spleens in various groups (n = 3, **$P < 0.01$, ***$P < 0.001$). (d–e) The percentage of Treg cells (CD3$^+$CD4$^+$Foxp3$^+$) in distant tumors and spleens after various treatments (n = 3, *$P < 0.05$, **$P < 0.01$, ***$P < 0.001$). (f) Cytokine levels of IFN-γ in serum after various treatments (n = 3, *$P < 0.05$, **$P < 0.01$).

distant tumors, with mice average survival times of 49.6 and 50.4 days, slightly longer than 41.6 day and 44.8 day for G3 and G4. In comparison, the immunotherapy induced by IR-R@LIP/PFOB + Laser + anti-PD-1 contributed to the most significant inhibitory effect on distant tumors, and led to the longest average survival time of 57.6 days (Fig. 7c and d). The results showed that the combined treatment in G7 could achieve the maximum therapeutic benefit, with the complete inhibition of primary tumor and a relative high tumor inhibition rate of distant tumors. Meanwhile, no significant body weight fluctuation was observed during the observation period (Fig. S11).

To further confirm the synergistic therapeutic effect, the primary tumor tissues in each group were subjected to H&E and TUNEL staining, and the metastatic tumor tissues were collected to analyze the expression of PCNA by immunofluorescence assay (Fig. 7e). As shown in images from H&E and TUNEL sections, the treatment of IR-R@LIP/PFOB + Laser + anti-PD-1 resulted in serious cell necrosis/apoptosis, while other treatments only lead to moderate or weak cell destruction. PCNA staining results showed proliferative activity of distant tumors was significantly inhibited after the IR-R@LIP/PFOB + Laser + anti-PD-1 treatment, proving that such treatment was highly effective in anti-tumor therapy.

3.7. Biosafety evaluation of IR-R@LIP/PFOB

In order to evaluate the potential systemic toxicity of IR-R@LIP/PFOB nanoplatforms, blood samples were collected for hematological assessment at 0, 3, 7, 14, and 30 days post IR-R@LIP/PFOB injection. The results of whole blood cell count, liver function markers, kidney function markers, and myocardial enzyme spectrum showed negligible differences among groups in different stages (Fig. S12a). H&E staining of major organs (heart, liver, spleen, lung, and kidney) also showed no obvious physiological abnormality (Fig. S12b). These results showed that the prepared IR-R@LIP/PFOB nanoplatforms possess excellent biosafety and biocompatibility.

4. Conclusion

In summary, an oxygen-carrying nanoplatform with immune stimulation and modulation functions was constructed for synergistic cancer PTT and immunotherapy. Ascribing to the unique prosperity of IR780, the prepared IR-R@LIP/PFOB could efficiently accumulate in 4T1 tumor cells, especially in mitochondria. Together with laser irradiation, the IR-R@LIP/PFOB showed high potentials in inducing ICD both in cellular level and 4T1 tumor-bearing mice model. Meanwhile, the IR-R@LIP/PFOB demonstrated efficient oxygen delivery owing to the high oxygen loading capacity of PFOB, resulting in the attenuation of tumor hypoxia *in situ*. Importantly, combination treatments of such immunogenic PTT and immune checkpoint blockade therapy could efficiently suppress tumor growth by eliciting potent anti-tumor immune response and reversing tumor immunosuppression. Moreover, attributing to the highly efficient therapeutic efficacy, as well as excellent biosafety and
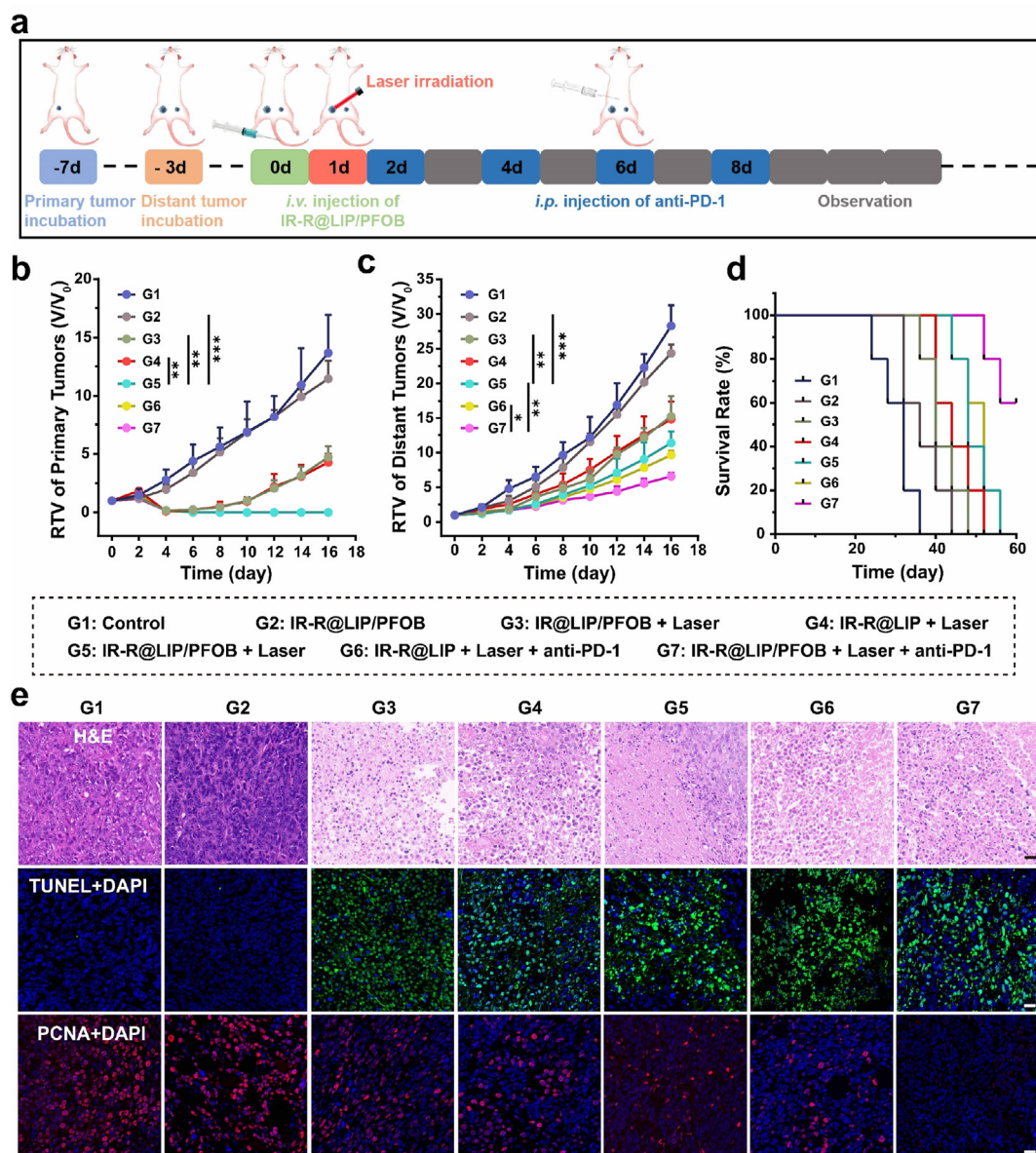
Fig. 7. *In vivo* **photothermal immunotherapy.** (a) Schematic illustration of the therapeutic process based on IR-R@LIP/PFOB. (b) RTV of the primary tumors and (c) distant tumors in different groups (n = 5, *$P < 0.05$, **$P < 0.01$, ***$P < 0.001$). (d) Relative survival rate of 4T1 tumor-bearing mice after various treatments (n = 5). (e) H&E, TUNEL, and PCNA staining of tumor slices collected from 4T1 tumor-bearing mice after various treatments (scale bar = 20 μm).

biocompatibility of these IR-R@LIP/PFOB nanoplatforms, IR-R@LIP/PFOB-based photothermal-immunotherapy holds great promise for cancer therapy.

Credit author statement:

Ju Huang: Methodology, Writing – original draft preparation, Investigation, Software, Writing-Reviewing and Editing. Xiaojing Leng: Methodology, Data curation, Writing – original draft preparation, Visualization. Tao Jiang: Methodology, Software, Validation. Lihong Xu: Methodology, Software. Jun Zheng: Methodology, Visualization, Investigation. Mingxiao Fang: Resources, Writing–review, Formal analysis. Jingxue Wang: Formal analysis, Writing-Reviewing. Zhigang Wang: Conceptualization, Project administration, Supervision, Funding acquisition. Liang Zhang: Conceptualization, Project administration, Supervision, Funding acquisition.

Declaration of competing interest

Data availability

Data will be made available on request.

Acknowledgements

Appendix A. Supplementary data

Supplementary data to this article can be found online at https://doi.org/10.1016/j.mtbio.2023.100555.

References

[1] T.N. Schumacher, R.D. Schreiber, Neoantigens in cancer immunotherapy, Science 348 (6230) (2015) 69–74.

[2] A.V. Finck, T. Blanchard, C.P. Roselle, G. Golinelli, C.H. June, Engineered cellular immunotherapies in cancer and beyond, Nat. Med. 28 (4) (2022) 678–689.

[3] Y. Zhang, Z. Zhang, The history and advances in cancer immunotherapy: understanding the characteristics of tumor-infiltrating immune cells and their therapeutic implications, Cell, Mol. Immunol. 17 (8) (2020) 807–821.

[4] G. Morad, B.A. Helmink, P. Sharma, J.A. Wargo, Hallmarks of response, resistance, and toxicity to immune checkpoint blockade, Cell 184 (21) (2021) 5309–5337.

[5] M.F. Sanmamed, L. Chen, A paradigm shift in cancer immunotherapy: from enhancement to normalization, Cell 175 (2) (2018) 313–326.

[6] J.M. Glanz, S.R. Newcomer, M.F. Daley, F. DeStefano, H.C. Groom, M.L. Jackson, B.J. Lewin, N.L. McCarthy, D.L. McClure, K.J. Narwaney, J.D. Nordin, O. Zerbo, Association between estimated cumulative vaccine antigen exposure through the first 23 months of life and non-vaccine-targeted infections from 24 through 47 months of age, JAMA 319 (9) (2018) 906–913.

[7] M. Saxena, S.H. van der Burg, C.J.M. Melief, N. Bhardwaj, Therapeutic cancer vaccines, Nat. Rev. 21 (6) (2021) 360–378.

[8] S.P. Kubli, T. Berger, D.V. Araujo, L.L. Siu, T.W. Mak, Beyond immune checkpoint blockade: emerging immunological strategies, Nat. Rev. 20 (12) (2021) 899–919.

[9] M. Zhang, X. Qin, Z. Zhao, Q. Du, Q. Li, Y. Jiang, Y. Luan, A self-amplifying nanodrug to manipulate the Janus-faced nature of ferroptosis for tumor therapy, Nanoscale Horiz 7 (2) (2022) 198–210.

[10] X. Ren, N. Wang, Y. Zhou, A. Song, G. Jin, Z. Li, Y. Luan, An injectable hydrogel using an immunomodulating gelator for amplified tumor immunotherapy by blocking the arginase pathway, Acta Biomater. 124 (2021) 179–190.

[11] S. Zhou, Q. Shang, N. Wang, Q. Li, A. Song, Y. Luan, Rational design of a minimalist nanoplatform to maximize immunotherapeutic efficacy: four birds with one stone, J. Contr. Release 328 (2020) 617–630.

[12] Z. Li, X. Lai, S. Fu, L. Ren, H. Cai, H. Zhang, Z. Gu, X. Ma, K. Luo, Immunogenic cell death activates the tumor immune microenvironment to boost the immunotherapy efficiency, Adv. Sci. 9 (22) (2022), e2201734.

[13] R. Guo, S. Wang, L. Zhao, Q. Zong, T. Li, G. Ling, P. Zhang, Engineered nanomaterials for synergistic photo-immunotherapy, Biomaterials 282 (2022), 121425.

[14] M. Chang, Z. Hou, M. Wang, C. Li, J. Lin, Recent advances in hyperthermia therapy-based synergistic immunotherapy, Adv. Mater. 33 (4) (2021), e2004788.

[15] W. Li, J. Yang, L. Luo, M. Jiang, B. Qin, H. Yin, C. Zhu, X. Yuan, J. Zhang, Z. Luo, Y. Du, Q. Li, Y. Lou, Y. Qiu, J. You, Targeting photodynamic and photothermal therapy to the endoplasmic reticulum enhances immunogenic cancer cell death, Nat. Commun. 10 (1) (2019) 3349.

[16] L. Huang, Y. Li, Y. Du, Y. Zhang, X. Wang, Y. Ding, X. Yang, F. Meng, J. Tu, L. Luo, C. Sun, Mild photothermal therapy potentiates anti-PD-L1 treatment for immunologically cold tumors via an all-in-one and all-in-control strategy, Nat. Commun. 10 (1) (2019) 4871.

[17] X. Li, J.F. Lovell, J. Yoon, X. Chen, Clinical development and potential of photothermal and photodynamic therapies for cancer, Nat. Rev. 17 (11) (2020) 657–674.

[18] Q. Chen, L. Xu, C. Liang, C. Wang, R. Peng, Z. Liu, Photothermal therapy with immune-adjuvant nanoparticles together with checkpoint blockade for effective cancer immunotherapy, Nat. Commun. 7 (2016), 13193.

[19] W. Yue, L. Chen, L. Yu, B. Zhou, H. Yin, W. Ren, C. Liu, L. Guo, Y. Zhang, L. Sun, K. Zhang, H. Xu, Y. Chen, Checkpoint blockade and nanosonosensitizer-augmented noninvasive sonodynamic therapy combination reduces tumour growth and metastases in mice, Nat. Commun. 10 (1) (2019) 2025.

[20] Y. Chao, C. Liang, H. Tao, Y. Du, D. Wu, Z. Dong, Q. Jin, G. Chen, J. Xu, Z. Xiao, Q. Chen, C. Wang, J. Chen, Z. Liu, Localized cocktail chemoimmunotherapy after in situ gelation to trigger robust systemic antitumor immune responses, Sci. Adv. 6 (10) (2020) eaaz4204.

[21] Z. Yang, D. Tao, W. Zhong, Z. Liu, L. Feng, M. Chen, Perfluorocarbon loaded fluorinated covalent organic polymers with effective sonosensitization and tumor hypoxia relief enable synergistic sonodynamic-immunotherapy, Biomaterials 280 (2022) 121250.

[22] J. Kopecka, I.C. Salaroglio, E. Perez-Ruiz, A.B. Sarmento-Ribeiro, S. Saponara, J. De Las Rivas, C. Riganti, Hypoxia as a driver of resistance to immunotherapy, Drug Resist. Updates 59 (2021), 100787.

[23] Z. Dong, C. Wang, Y. Gong, Y. Zhang, Q. Fan, Y. Hao, Q. Li, Y. Wu, X. Zhong, K. Yang, L. Feng, Z. Liu, Chemical modulation of glucose metabolism with a fluorinated caco(3) nanoregulator can potentiate radiotherapy by programming antitumor immunity, ACS Nano 16 (9) (2022) 13884–13899.

[24] A. Christofides, L. Strauss, A. Yeo, C. Cao, A. Charest, V.A. Boussiotis, The complex role of tumor-infiltrating macrophages, Nat. Immunol. 23 (8) (2022) 1148–1156.

[25] S. Devalaraja, T.K.J. To, I.W. Folkert, R. Natesan, M.Z. Alam, M. Li, Y. Tada, K. Budagyan, M.T. Dang, L. Zhai, G.P. Lobel, G.E. Ciotti, T.S.K. Eisinger-Mathason, I.A. Asangani, K. Weber, M.C. Simon, M. Haldar, Tumor-derived retinoic acid regulates intratumoral monocyte differentiation to promote immune suppression, Cell 180 (6) (2020) 1098–1114.

[26] I. Vitale, G. Manic, L.M. Coussens, G. Kroemer, L. Galluzzi, Macrophages and metabolism in the tumor microenvironment, Cell Metabol. 30 (1) (2019) 36–50.

[27] A.T. Henze, M. Mazzone, The impact of hypoxia on tumor-associated macrophages, J. Clin. Invest. 126 (10) (2016) 3672–3679.

[28] C. Li, X. Xu, S. Wei, P. Jiang, L. Xue, J. Wang, Tumor-associated macrophages: potential therapeutic strategies and future prospects in cancer, J. Immunother. Cancer 9 (1) (2021), e001341.

[29] X. Song, L. Feng, C. Liang, K. Yang, Z. Liu, Ultrasound triggered tumor oxygenation with oxygen-shuttle nanoperfluorocarbon to overcome hypoxia-associated resistance in cancer therapies, Nano Lett. 16 (10) (2016) 6145–6153.

[30] X. Liang, X. Chen, M. Bhattarai, S. Hameed, Z. Dai, Perfluorocarbon@Porphyrin nanoparticles for tumor hypoxia relief to enhance photodynamic therapy against liver metastasis of colon cancer, ACS Nano 14 (10) (2020) 13569–13583.

[31] J. Huang, L. Zhang, W. Zhou, J. Wang, R. Zhang, Z. Wang, H. Ran, P. Li, R. Li, Dual mitigation of immunosuppression combined with photothermal inhibition for highly effective primary tumor and metastases therapy, Biomaterials 274 (2021), 120856.

[32] C. Ji, J. Si, Y. Xu, W. Zhang, Y. Yang, X. He, H. Xu, X. Mou, H. Ren, H. Guo, Mitochondria-targeted and ultrasound-responsive nanoparticles for oxygen and nitric oxide codelivery to reverse immunosuppression and enhance sonodynamic therapy for immune activation, Theranostics 11 (17) (2021) 8587–8604.

[33] H. Tian, L. Zhou, Y. Wang, E.C. Nice, C. Huang, H. Zhang, A targeted nanomodulator capable of manipulating tumor microenvironment against metastasis, J. Contr. Release 348 (2022) 590–600.

[34] L. Zhang, H. Yi, J. Song, J. Huang, K. Yang, B. Tan, D. Wang, N. Yang, Z. Wang, X. Li, Mitochondria-targeted and ultrasound-activated nanodroplets for enhanced deep-penetration sonodynamic cancer therapy, ACS Appl. Mater. Interfaces 11 (9) (2019) 9355–9366.

[35] W.Y. Wang, Y.X. Cao, X. Zhou, B. Wei, Delivery of folic acid-modified liposomal curcumin for targeted cervical carcinoma therapy, Drug Des. Dev. Ther. 13 (2019) 2205–2213.

[36] F. Lu, Z. Li, Y. Sheng, Y. Ma, Y. Yang, Y. Ren, Z. Su, R. Yu, S. Zhang, Thermal-triggered packing of lipophilic NIR dye IR780 in hepatitis B core at critical ionic strength and cargo-host ratio for improved stability and enhanced cancer phototherapy, Biomaterials 276 (2021), 121035.

[37] F. Tian, S. Wang, K. Shi, X. Zhong, Y. Gu, Y. Fan, Y. Zhang, M. Yang, Dual-depletion of intratumoral lactate and atp with radicals generation for cascade metabolic-chemodynamic therapy, Adv. Sci. 8 (24) (2021), e2102595.

[38] C. Zhao, Y. Tong, X. Li, L. Shao, L. Chen, J. Lu, X. Deng, X. Wang, Y. Wu, Photosensitive nanoparticles combining vascular-independent intratumor distribution and on-demand oxygen-depot delivery for enhanced cancer photodynamic therapy, Small 14 (12) (2018), e1703045.

[39] D. Sheng, T. Liu, L. Deng, L. Zhang, X. Li, J. Xu, L. Hao, P. Li, H. Ran, H. Chen, Z. Wang, Perfluorooctyl bromide & indocyanine green co-loaded nanoliposomes for enhanced multimodal imaging-guided phototherapy, Biomaterials 165 (2018) 1–13.

[40] X. Guo, N. Yang, W. Ji, H. Zhang, X. Dong, Z. Zhou, L. Li, H.M. Shen, S.Q. Yao, W. Huang, Mito-bomb: targeting mitochondria for cancer therapy, Adv. Mater. 33 (43) (2021), e2007778.

[41] E.E. Sweeney, J. Cano-Mejia, R. Fernandes, Photothermal therapy generates a thermal window of immunogenic cell death in neuroblastoma, Small 14 (20) (2018), e1800678.

[42] X. Zhang, J. Tang, C. Li, Y. Lu, L. Cheng, J. Liu, A targeting black phosphorus nanoparticle based immune cells nano-regulator for photodynamic/photothermal and photo-immunotherapy, Bioact. Mater. 6 (2) (2021) 472–489.

[43] H. Fang, B. Ang, X. Xu, X. Huang, Y. Wu, Y. Sun, W. Wang, N. Li, X. Cao, T. Wan, TLR4 is essential for dendritic cell activation and anti-tumor T-cell response enhancement by DAMPs released from chemically stressed cancer cells, Cell, Mol. Immunol. 11 (2) (2014) 150–159.

[44] D.V. Krysko, A.D. Garg, A. Kaczmarek, O. Krysko, P. Agostinis, P. Vandenabeele, Immunogenic cell death and DAMPs in cancer therapy, Nat. Rev. Cancer 12 (12) (2012) 860–875.

[45] J.R. Mora, M. Iwata, B. Eksteen, S.Y. Song, T. Junt, B. Senman, K.L. Otipoby, A. Yokota, H. Takeuchi, P. Ricciardi-Castagnoli, K. Rajewsky, D.H. Adams, U.H. von Andrian, Generation of gut-homing IgA-secreting B cells by intestinal dendritic cells, Science 314 (5802) (2006) 1157–1160.

[46] H. Cheng, X. Fan, E. Ye, H. Chen, J. Yang, L. Ke, M. You, M. Liu, Y.W. Zhang, Y.L. Wu, G. Liu, X.J. Loh, Z. Li, Dual tumor microenvironment remodeling by glucose-contained radical copolymer for MRI-guided photoimmunotherapy, Adv. Mater. 34 (25) (2022), e2107674.

[47] A. Weidemann, R.S. Johnson, Biology of HIF-1alpha, Cell Death Differ. 15 (4) (2008) 621–627.

[48] J. Rius, M. Guma, C. Schachtrup, K. Akassoglou, A.S. Zinkernagel, V. Nizet, R.S. Johnson, G.G. Haddad, M. Karin, NF-kappaB links innate immunity to the hypoxic response through transcriptional regulation of HIF-1alpha, Nature 453 (7196) (2008) 807–811.

[49] L. You, W. Wu, X. Wang, L. Fang, V. Adam, E. Nepovimova, Q. Wu, K. Kuca, The role of hypoxia-inducible factor 1 in tumor immune evasion, Med. Res. Rev. 41 (3) (2021) 1622–1643.

[50] C. Lu, F. Zhou, S. Wu, L. Liu, D. Xing, Phototherapy-induced antitumor immunity: long-term tumor suppression effects via photoinactivation of respiratory chain

oxidase-triggered superoxide anion burst, Antioxidants Redox Signal. 24 (5) (2016) 249–262.

[51] X. Chen, Z. Jia, Y. Wen, Y. Huang, X. Yuan, Y. Chen, Y. Liu, J. Liu, Bidirectional anisotropic palladium nanozymes reprogram macrophages to enhance collaborative chemodynamic therapy of colorectal cancer, Acta Biomater. 151 (2022) 537–548.

[52] D. Chen, J. Xie, R. Fiskesund, W. Dong, X. Liang, J. Lv, X. Jin, J. Liu, S. Mo, T. Zhang, F. Cheng, Y. Zhou, H. Zhang, K. Tang, J. Ma, Y. Liu, B. Huang, Chloroquine modulates antitumor immune response by resetting tumor-associated macrophages toward M1 phenotype, Nat. Commun. 9 (1) (2018) 873.

[53] A. Savina, S. Amigorena, Phagocytosis and antigen presentation in dendritic cells, Immunol. Rev. 219 (2007) 143–156.

[54] C.D. Castro, A.M. Luoma, E.J. Adams, Coevolution of T-cell receptors with MHC and non-MHC ligands, Immunol. Rev. 267 (1) (2015) 30–55.